DOI: ADD DOINUMBER HERE

Numerical analysis of surface jets for load alleviation on transport aircraft

Florian Siebert[⋆,†], *Till Strothteicher*[⋆,§], *and André Bauknecht*[⋆,†]
[⋆]*Cluster of Excellence SE*^{2}*A - Sustainable and Energy Efficient Aviation, Technische Universität Braunschweig*
38108 Braunschweig, Germany
florian.siebert@tu-braunschweig.de · till.strothteicher@dlr.de
[†]Institute of Fluid Mechanics, TU Braunschweig
[§]DLR Institute of Flight Systems

Abstract

Effective alleviation of aerodynamic peak loads — caused by gusts or maneuvers — allows significant wing-structure mass reduction and lower energy consumption. Traditional control surfaces, like trailing-edge flaps, are limited by deflection rates, whereas fluidic actuators, such as wall-normal surface jets, use pressurized air to achieve much faster response. This study selects and evaluates a surface-jet design for elastic 3D aircraft wings. First, a 2D RANS-based parametric study shows that using narrow slots of 0.05 % chord width cuts mass flow requirements by 40 % at fixed pressure ratios, compared to prior designs, despite lower efficiency at supersonic jet speeds. Chordwise positioning at $x/c = 0.8$ yields greater lift reduction on a stiff 2D wing section, while $x/c = 0.6$ enhances decoupling between lift and pitching moment control, which is beneficial for flexible wings and outboard locations. Two selected actuator geometries were evaluated over varying Reynolds numbers, Mach numbers, and angles of attack to generate a CFD dataset from which a reduced-order model is derived. Implemented in a low-fidelity aeroelastic framework, results confirm that chordwise placement at $x/c = 0.6$ balances lift control and pitching moment, achieving 20 % wing-root bending-moment reduction compared to the trim load at less than 1.5 kg/s mass flow, while the most effective spanwise location is at 75 % span.

1. Introduction

The ambitious goal of reducing the climate impact of global aviation can only be met by introducing new aircraft configurations that integrate sustainable propulsion concepts as well as novel airframe technologies.[1] These airframe technologies aim to reduce drag, structural weight and ultimately the fuel consumption of future transport aircraft. A reduction of wing structural weight can be achieved by alleviating peak aerodynamic loads that act on the aircraft structure during gust encounters and flight maneuvers. These flight conditions are sizing for the wing structure according to certification requirements.[2] Maneuver and gust induced loads can be alleviated either by passive structural means or by actively controlling the distribution of aerodynamic forces during these events. Several conceptual design studies considering load alleviation in the preliminary design phase together with multidisciplinary optimization demonstrate the potential of active load control to reduce fuel burn by approximately 10 % compared to state of the art aircraft.[1,3,4]

Passive load alleviation exploits the structural response of a wing to induced loads, e.g. the coupling of the upward wing bending to a nose-down torsional deformation, thereby reducing lift at the outboard wing section. The load-alleviating structural response can be enhanced by implementing geometric non-linearities that increase wing bending after a critical load-factor is exceeded.[5,6] Active systems are required to achieve a higher level of load alleviation than by a passive approach alone. The combination of trailing edge flaps for redistributing lift and thus reducing wing root bending moment and leading edge flaps for controlling torsional moments showed high potential for load alleviation on an elastic wing in quasi-steady maneuver flight.[7] Significant reductions of dynamic gust loads, however, can only be achieved using high actuation rates of the flaps that are challenging to realize.[8,9] Further drawbacks of using control surfaces for load alleviation besides their limited deployment rates are the heavy electro-mechanical actuation system and its space requirement that can prevent implementation in the slender outer sections of high aspect ratio wings. In addition, mechanical systems run the risk of getting stuck in deployed position and undergo frequent and dynamic load changes that can lead to fatigue of the system.

Fluidic actuators have the potential to overcome most of these challenges. Using a pressurized air system, it was demonstrated that very short onset times could be realized due to the system's highly reduced inertia,[10,11] which

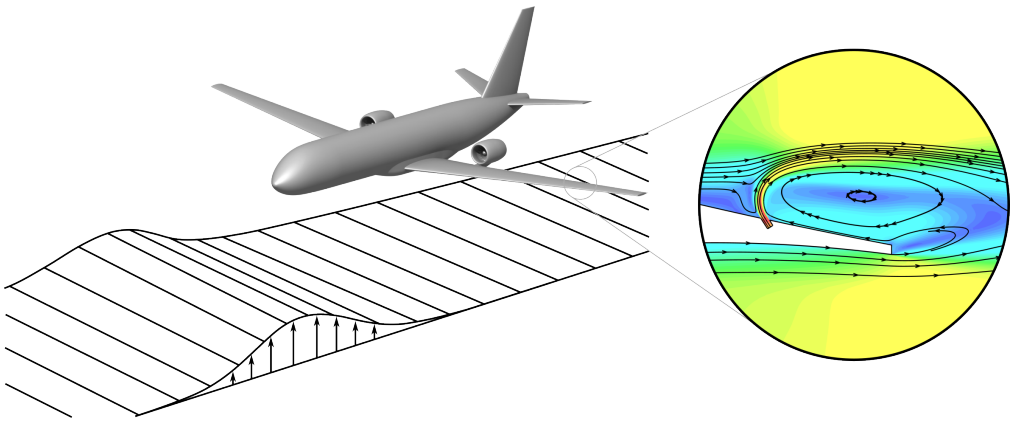

Figure 1: Concept sketch of a surface jet for gust load alleviation integrated into a transport aircraft wing.

becomes even more relevant in case of delayed gust detection.[12] The air supply system including tubes and fast switching proportional valves is potentially lighter and easier to integrate in small internal volumes of slender wings, and offers a better fail-safe design as blowing requires the continuous input of energy to be active. A systematic study by Khalil et al.[13] on a transonic airfoil identified suitable flow control concepts for load alleviation and demonstrated their higher control authority compared to (micro-)mechanical concepts. Among those concepts, the surface jet actuator showed the highest lift reduction potential of about 60 % of the gust-induced lift under transonic conditions[12] and was therefore selected for the present study. This actuator consists of a thin air jet that is issued from an orifice on the upper side of the surface under a certain angle against the outer flow, thus creating a separation region downstream of the jet location. As shown in the concept sketch in Fig. 1, the flow deflection at the trailing edge is reduced by the separation, which results in an effective de-camber of the airfoil and consequently lower airfoil lift.

The mass flow required in the 2D study by Khalil et al.[12] to alleviate 50 % of the additional lift induced by a gust of 70 m length sums up to 0.23 kg per meter span with a peak mass flow of 1.2 kg/s for a representative wing section of 4 m chord length. These values indicate the necessity to further reduce the mass flow demand of the actuator to enable the application of this technology to future transport aircraft. A few studies[12, 14, 15] provide guidance on actuator design for high mass flow efficiency and integration on elastic three dimensional wings, but omit relevant aspects. Regarding the actuator geometry in a 2D wing section, the enhancement of control authority by tilting the jet forward is well described,[14] but discussions of the jet width effect stay perfunctory. Especially an investigation of chordwise position and its influence on the ratio of lift control over change of pitching moment is missing, which is particularly relevant for the actuator integration on a flexible wing with aeroelastic effects. A surface jet implemented on the outer 25 % of a tapered wing showed good capabilities of reducing wing root bending moment during gust encounters, including the plunging and first bending mode in the aeroelastic simulation.[15] Considerations of aeroelastic effects including torsional modes and discussions of the impact of spanwise and chordwise positioning and actuator induced pitching moment on its aeroelastic effectiveness are currently missing in literature.

The present work aims to fill this gap in three consecutive steps. First, investigations on 2D actuator design parameters are shown on a representative wing section of a civil transport aircraft. The study focuses on small slot widths for high-velocity jets with low mass flow demand. Special emphasis is put on the influence of chordwise positioning on control authority over lift and pitching moment. In a second step, the suggested actuator design is tested under various flight conditions and a reduced-order model is derived. This model serves as an input for low-fidelity aeroelastic simulations of the full aircraft with different actuator configurations integrated on the wing. During this third step, initial conclusions are drawn on the actuator integration strategy for high aeroelastic effectiveness.

2. Numerical methods

2.1 Research configuration and operating conditions

A medium range aircraft developed within the Cluster of Excellence SE^{2}A was used as research configuration for the present study. Details on the conceptual design process of this aircraft including design considerations, top-level aircraft requirements and implemented sustainable aviation technologies are given by Karpuk et al.[16] The design flight conditions with an altitude of 7650 m (25100 ft) and a Mach number of $M_\infty = 0.71$ were chosen to be lower and slower than for conventional medium-range aircraft to drastically reduce the climate impact of contrails. The aircraft features

backward-swept, fully turbulent wings and over-wing mounted engines as depicted in Fig. 1. The wings have an aspect ratio of $\lambda = b^2/S_{\text{wing}} = 12.11$ with a span of $b = 43.4\,\text{m}$, and a leading edge sweep of $\varphi_{\text{LE}} = 16°$. The wing design is based on the DLR-F15 airfoil[17] with a root chord of $c_{\text{root}} = 6.3\,\text{m}$ with 13 % relative thickness and a tip chord of $c_{\text{tip}} = 1.63\,\text{m}$ with 10.5 % relative thickness.

A representative wing section was derived for the 2D simulations in this study based on the mean aerodynamic chord of $c_{\text{MAC}} = 4.1\,\text{m}$ and 12 % relative thickness. Infinite swept wing analogy was applied to this section to account for sweep effects. The sweep transformation

$$\begin{aligned} c_{2\text{D}} &= c_{\text{MAC}} \cdot \cos(\varphi_{c/4}) \\ M_{2\text{D}} &= M_\infty \cdot \cos(\varphi_{c/4}) \\ Re_{2\text{D}} &= Re_\infty \cdot \cos^2(\varphi_{c/4}) \end{aligned} \tag{1}$$

is based on the quarter-chord sweep of $\varphi_{c/4} = 13.8°$ due to the high subsonic character of the flow regime. This results in a scaling of the chord length to $c_{2\text{D}} = 3.98\,\text{m}$, which increases the relative thickness of the transformed airfoil to $t/c = 12.36\,\%$. The design Mach number and the Reynolds number based on mean aerodynamic chord of $Re_{\infty,\text{MAC}} = 32 \times 10^6$ are scaled to $M_{2\text{D}} = 0.69$ and $Re_{2\text{D}} = 30.2 \times 10^6$.

2.2 Flow control concept

Active flow control through surface jet blowing was applied in this study by releasing pressurized air from a duct inside the airfoil. In the first part of the study (see Sec. 3.1), this duct has parallel walls as sketched in Fig. 2. The variation of geometric parameters includes ten different chordwise positions between $x/c = 0.3 - 0.95$, nine different slot widths within $w/c = 0.025\,\% - 0.5\,\%$ and six tilt angles relative to the local wall normal of $\theta_{\text{duct}} = 0° - 75°$ against the flow. The jet blowing was realized by imposing an actuation boundary condition on the bottom surface of the duct (hereafter referred to as "inlet"). The boundary condition requires the prescription of total temperature and total pressure of the fluid at that inlet. A variation of jet total temperature can have noticeable effects on the actuator performance.[10,18] To exclude these effects, the total temperature was set to a fixed value of 356 K, which was chosen as an average between ambient temperature at cruise altitude and typical bleed air temperatures. The prescribed total pressure is thus the primary control variable to set a specific blowing rate. The correlation between jet pressure and blowing rate in terms of jet momentum is later shown in Fig. 7e. For subsonic flow conditions, the CFD solver calculates the local static pressure at the inlet by extrapolation from the flow field onto the edge of the computational domain. Supersonic outflow conditions at high blowing intensities can be prescribed as well, which require the additional prescription of static pressure on the boundary surface due to the supercritical nature of the flow. The static pressure in this case is a variable of free choice and was set to free stream pressure. For all blowing rates, it is assumed that an ideal nozzle upstream of the inlet operates in its design point to create these flow conditions. Off-design performance of the nozzle is therefore neglected to show the hypothetical best performance of each duct geometry.

For the second part of the study, which is presented in Sec. 3.2, the best suited geometric parameters from the first part were selected and kept constant, and the actuator's performance is investigated across the flight envelope. A convergent nozzle is used here instead of a rectangular duct to account for nozzle off-design conditions. The flow conditions on the inlet are always subsonic for all blowing rates. High blowing rates lead to a chocked nozzle and an under-expanded jet. A discussion on the choice of a convergent nozzle is given in Sec. 3.1. Examples of both a rectangular and a convergent duct are shown in Fig. 3.

The blowing intensity is quantified by the mass flow $\dot{m}$, the jet momentum $\dot{I} = \dot{m} v_{\text{jet}}$ and the kinetic jet power $\dot{E}_{\text{jet,kin}} = 1/2 \dot{m} v_{\text{jet}}^2$. The dimensionless mass flow coefficient C_Q, momentum coefficient C_μ, and kinetic power coefficient $C_{P,\text{kin}}$ can be calculated from these quantities by referring them to free stream properties according to Eq. 2. The pressure terms were taken into account for the computation of the momentum coefficient in case of an underexpanded jet, where A_{jet} is the cross-sectional area of the nozzle throat. Mass flow, jet momentum and jet power were computed by integrating the corresponding fluxes across the jet exit surface. For the convergent nozzle, this surface was placed at the nozzle throat, as indicated in Fig. 3 by a dashed orange line.

$$\begin{aligned} C_Q &= \frac{\dot{m}}{\rho_\infty v_\infty S_{\text{ref}}} \\ C_\mu &= \frac{\dot{m} v_{\text{jet}} + A_{\text{jet}}(p_{\text{jet}} - p_\infty)}{\frac{1}{2}\rho_\infty v_\infty^2 S_{\text{ref}}} \\ C_{P,kin} &= \frac{\dot{m} v_{\text{jet}}^2}{\rho_\infty v_\infty^3 S_{\text{ref}}} \end{aligned} \tag{2}$$

A discussion of the technical-physical interpretation of these coefficients is given by Radespiel et al.[19] The momentum coefficient, due to its normalization, can be seen as an additional drag component that appears due to a loss of engine thrust caused by the extraction of bleed air. The power coefficient corresponds to the electrical or mechanical power required to run an idealized compressor for air supply. The power added by a compressor to the blowing air can be determined from a stream tube running from a point at free stream conditions to the jet exit. It follows that $P_{\text{Compressor}} = \dot{m} c_P (T_{t,\text{jet}} - T_{t,\infty})$ with the heat capacity c_P. In this study however, the total jet temperature $T_{t,\text{jet}}$ was kept constant as explained above, so that $P_{\text{Compressor}} \propto \dot{m}$. Therefore, only the kinetic component of the jet power is used here to quantify the compressor power.

The reaction force of the ejected air is taken into account for the calculation of aerodynamic lift and drag by adding the inverted vector of jet momentum to the solver forces. The pitching moment relative to the quarter chord is corrected by adding the z-component of the jet momentum multiplied with its lever arm $(x - 0.25c)$, while the x-component is disregarded due to its negligible contribution. The influence of the reaction force on lift is in the order of 2 % and approximately 10 % for the pitching moment.

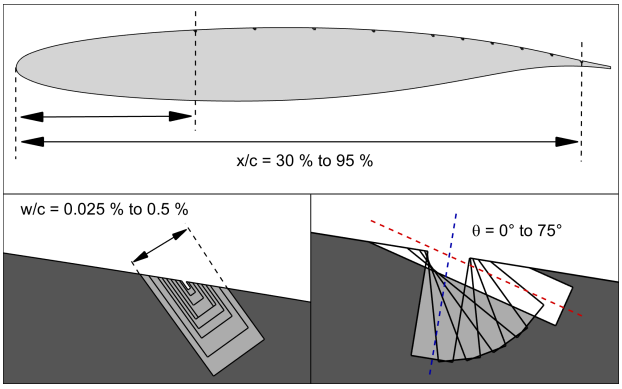

Figure 2: Actuator geometry

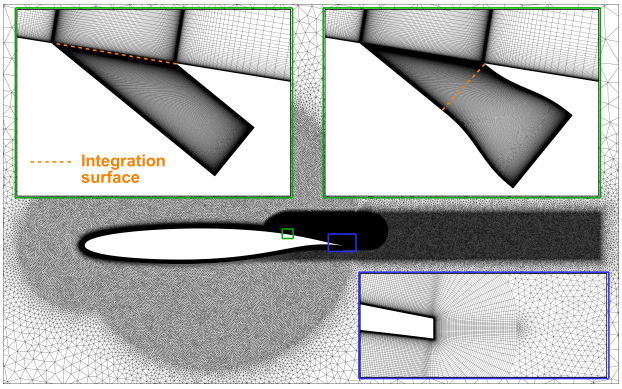

Figure 3: Numerical grids

2.3 CFD Set-up

The unstructured finite volume solver TAU developed by the German Aerospace Center (DLR)[20] was used to solve the RANS equations. A second order central scheme with scalar dissipation was used for spatial discretization and an implicit Backward-Euler scheme for time integration with local time-stepping. Cauchy tolerances of 10^{-6} for lift, drag, and pitching moment were used to control convergence of the simulations. Turbulence modeling was realized by the one-equation Spalart-Allmaras model in its modified version from 2012.[21] All surfaces of the airfoil are treated as turbulent walls. In case of active blowing, the actuation boundary condition described in Sec. 2.2 is imposed on the bottom surface of the duct.

Two versions of a sample 2D grid with a rectangular and convergent duct of 0.05%c width at $x/c = 0.8$ and a tilt angle of 60° are shown in Fig. 3. A CAD model of the airfoil with a fully parameterized duct was constructed in the commercial CAD software CATIA® V5. The exported geometry was discretized in an automatic mesh generation process using Fidelity Pointwise® with Glyph scripting language. A hybrid mesh set-up is used with a structured mesh to resolve the boundary layer flow and an unstructured triangle mesh for the outer grid domain. The boundary layer mesh resembles an O-topology with a blunt trailing edge and was generated by wall normal extrusion with a first cell height iteratively selected to fulfill the $y_1^+ \leq 1$ condition for turbulent boundary layer resolution under all investigated flight conditions. The cell density of the unstructured grid is increased around the slot, the trailing edge and in the region of anticipated separated flow.

A grid sensitivity study was conducted based on the geometry used in a previous study.[12] Three grids (coarse, medium and fine) were initially created with a refinement factor of 2 applied between two levels. A fourth and final grid was subsequently created based on the experience with the initial grids. Some characteristic properties and the simulation results of all four grids are shown in Tab. 1. The final grid features the spacings from the fine grid, which shows significantly improved simulation convergence due to low disturbance levels around the slot, and the extrusion settings from the medium grid that provides sufficient boundary layer resolution. The grids were tested at three different blowing conditions: No blowing, moderate blowing with subsonic jet velocity at $C_\mu = 0.01$, and strong blowing with supersonic jet velocity at $C_\mu = 0.025$. All three conditions show very similar quantitative trends of which the one for moderate blowing is shown in Tab. 1. The final grid is considered sufficiently fine, as the sensitivity with respect to the medium grid is two orders of magnitude below the expected sensitivity to the geometric parameter variations.

Table 1: Grid sensitivity study - grid properties and results for $C_\mu = 0.01$

Grid level	y_1/m	extrusion steps	spacing in separation region	n_{nodes}	Δc_l [a]	Δc_d [a]	$\Delta c_{m,y}$ [a]
coarse	$6 \cdot 10^{-6}$	50	0.02 m	45 k	$-7.8 \cdot 10^{-3}$	$-6.1 \cdot 10^{-5}$	$1.7 \cdot 10^{-3}$
medium	$3 \cdot 10^{-6}$	100	0.01 m	157 k	$-1.5 \cdot 10^{-3}$	$-2.2 \cdot 10^{-5}$	$3.9 \cdot 10^{-4}$
final	$3 \cdot 10^{-6}$	100	0.005 m	382 k	$2.7 \cdot 10^{-5}$	$5.0 \cdot 10^{-6}$	$-3.3 \cdot 10^{-6}$
fine	$1.5 \cdot 10^{-6}$	200	0.005 m	568 k	-	-	-

[a]Differences with respect to the finest grid level

2.4 Aeroelastic framework

Complementary to the high-fidelity CFD simulations, an aeroelastic flight dynamics framework was employed to evaluate the performance of the actuator on a 3D wing with aeroelastic deformation for different actuator positions. The open-source framework[22,23] features a nonlinear unsteady model of an F-15 airfoil to describe the wing aerodynamics. Spanwise downwash is considered using a nonlinear steady lifting line method. Structural dynamics are modeled based on the mode displacement method. Furthermore, aerodynamic and structural models are coupled with constant transformation matrices as well as nonlinear transformations for the inflow.

The actuator performance is evaluated in this framework for the configuration presented in Sec. 2.1. Figure 4 shows the available actuators of the aircraft: There are three sets of conventional ailerons with a depth of 20 % local chord and three sets of surface jets positioned at either $x/c = 0.6$ or $x/c = 0.8$. Figure 4 highlights only the $x/c = 0.6$ surface jets for clarity. Actuators are implemented in the framework by modifying the local lift, moment and drag coefficients of the respective wing section. Deflection dynamics are implemented using second order dynamic models with appropriate bandwidths and damping ratios (40°/s and 100°/s for the −3 dB bandwidth of the ailerons[24] and surface jets,[14] respectively, and both with a damping ratio of 1). Unsteady aerodynamic effects through the deflection of ailerons are modeled with the method presented by Leishman.[25]

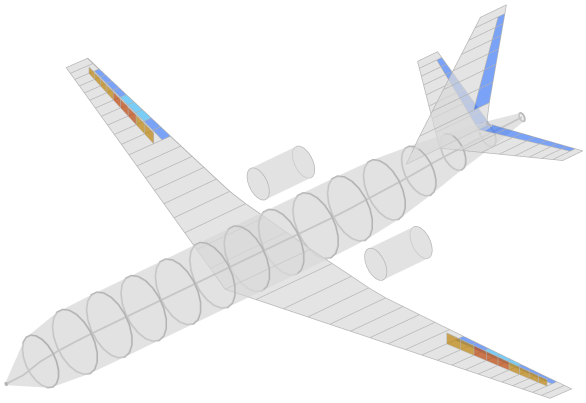

Figure 4: SE²A Mid-Range Aircraft, primary control surfaces in blue, surface jets positioned at $x/c = 0.6$ in orange

The quasi-steady change of the local aerodynamic coefficients $\Delta c_X = \left[\Delta c_l,\ \Delta c_{m,y},\ \Delta c_d\right]^T$ through a surface jet actuation is approximated using parameterized candidate functions Δc_X^{Fit}. These are fitted to the respective CFD data Δc_X^{CFD}, ensuring smooth aerodynamic coefficient gradients, which is beneficial for load alleviation controller design with linearized models. The candidate function is parameterized by eight fitting parameters $\mathbf{p}^{Fit} = [p_1, p_2, ..., p_8]$, and is fitted to Δc_X^{CFD} for each Mach number separately using a least squares approach with a nonlinear generalized reduced gradient solver. Mass flow and angle of attack effects are modeled separately.

$$\Delta c_X^{Fit}(\dot{m}, \alpha, \mathbf{p}^{Fit}) = \Delta c_{X,\dot{m}}(\dot{m}, \mathbf{p}^{Fit})\ \Delta c_{X,\alpha}(\alpha, \mathbf{p}^{Fit}) \tag{3}$$

The candidate function is set up to best represent the change in lift coefficient, but is used for all aerodynamic coefficients. The change in lift coefficient over increasing $\dot{m}$ shows a bilinear trend in the CFD data (later shown in Fig. 17

and Fig. 16). Hence, the mass flow characteristic is modeled by two linear functions and a transition function

$$\Delta c_{X,\dot{m}}(\dot{m}, \mathbf{p}^{Fit}) = \dot{m} p_1 \left(1 - F(\dot{m}, \mathbf{p}^{Fit})\right) + (\dot{m} - (p_2 + p_4))\, p_5 F(\dot{m}, \mathbf{p}^{Fit}) \tag{4}$$

where $F(\dot{m}, \mathbf{p}^{Fit})$ defines the transition from one linear function to the other:

$$F(\dot{m}, \mathbf{p}^{Fit}) = \frac{1}{2}(1 + \tanh((\dot{m} - p_2)p_3)) \tag{5}$$

The bilinear behavior is caused by the nozzle design, and the transition is approximately at the mass flow for which the nozzle throat flow becomes sonic. This is discussed subsequently in Sec. 3.1. Increasing the angle of attack generally leads to a larger change in lift coefficient, up until the flow separation influences the jet (later shown in Fig. 12 and Fig. 13). Equation 6 models this effect.

$$\Delta c_{X,\alpha}(\alpha, \mathbf{p}^{Fit}) = 1 + p_6\alpha - \exp(p_7(\alpha - p_8)) \tag{6}$$

3. Results

3.1 Design study

In the first part of this study, a variation of the two-dimensional jet duct geometry was carried out (see Fig. 2) to identify a suitable configuration for the present operating conditions. The goal of this step is to investigate sensitivities regarding flow control input and pitching moment effect with respect to the actuator geometry. The initial geometry was taken from Khalil et al.[12] and features a duct of $0.025\%c$ width at a chordwise position of $95\%c$ and tilted with an angle of 45° relative to the local wall normal against the flow direction. In a first step, the chordwise position was varied between $x/c = 0.3 - 0.95$ at constant slot width and tilt angle. The aftmost limit of the chordwise position was chosen to ensure integrability in the trailing edge.

Results of the actuator performance in terms of lift change over momentum coefficient for different actuator positions are shown in Fig. 5a. The lift reduction increases with higher momentum coefficients for all cases, but with a decreasing slope due to saturation effects. The achieved lift change at a specific blowing rate increases for more aft slot positions until $x/c \approx 0.75 - 0.8$ and decreases again slightly for $x/c > 0.8$. An examination of the flow field of actuators located in the front half of the airfoil reveals that the separated flow created by moderate blowing rates reattaches after $\Delta x \approx 0.2c$. The lift change results from the thick and weakened boundary layer on the upper side of the airfoil that causes a virtual de-camber of the airfoil with corresponding lift reduction. The strong effect of separated trailing edge flow is missing, which explains the poor performance of the slots at $x/c \leq 0.5$. The blowing rate at which full separation of the flow between slot and trailing edge occurs decreases for further aft located slots until at $x/c = 0.8$ even the smallest investigated jet momentum of $C_\mu = 0.001$ leads to full detachment of the flow.

The lift change factor $|\Delta c_l|/C_\mu$ is shown in Fig. 5b for specific target-$|\Delta c_l|$ values. The selected target lift changes of $|\Delta c_l| = 0.25 - 0.45$ correspond to the expected range of required lift reductions based on preliminary studies of critical gust loads on the reference aircraft configuration. The lift change factor is derived here as the absolute value of the commonly defined lift gain factor $\Delta c_l/C_\mu$ and quantifies the efficiency of the flow control by relating the achieved lift reduction to its cost in terms of jet momentum that has to be provided by the air supply system. It can be seen in Fig. 5b that maximum values of 100 to 170 can be achieved in the desired lift reduction range by actuators located at $x/c = 0.75 - 0.8$. These lift change factors are 50 % higher than those of a comparable surface jet implemented by Khalil et al.[13] due to more favorable positioning and tilting of the jet. On the other hand, they still lie well below lift gain factors achieved by Coanda actuators, which are, however, limited to lift reductions of about $\Delta c_l \approx -0.4$ under comparable conditions.[12] The observation of an optimal chordwise position for lift reduction at around $x/c = 0.75 - 0.8$ is in contrast to experimental results by Al-Battal et al.[26] They found for a symmetric NACA0012 model operated at low-speed conditions ($Re = 6.6 \times 10^5$, $M = 0.06$) that lift reductions at moderate angles of attack are higher the closer the jet is located to the trailing edge. However, flow field visualizations and pressure measurements of their model show that different pressure gradients and stall mechanisms are relevant for the low-speed tests compared to transonic airfoils under cruise flight conditions.

Particular attention is paid in this study on the control authority on both lift and pitching moment with regard to aeroelastic control effectiveness on flexible wings. Fig. 6 depicts the change of quarter chord pitching moment $\Delta c_{m,y}$ over change of lift for the investigated chordwise actuator locations. Each curve represents the performance of one actuator geometry for different blowing intensities, corresponding to the respective curves in Fig. 5a. The jet momentum coefficient is indicated by the contour plot and truncated at $C_\mu = 0.01$ for better readability. Starting at zero change in lift and pitching moment for zero jet momentum, the pitching moment of all geometries experiences a nose-up (positive) alteration as the lift reduces with increasing jet momentum. It becomes obvious again that the jets located

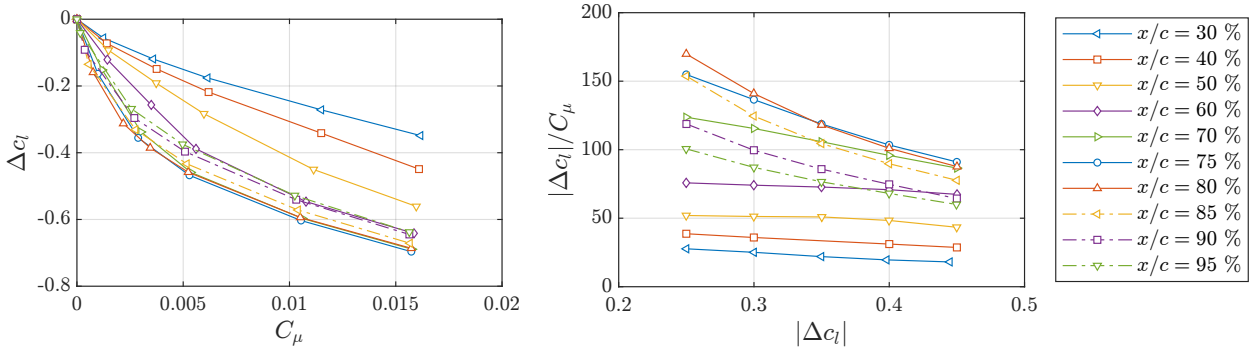

(a) Lift change over momentum coefficient

(b) Lift change factor over Δc_l

Figure 5: Steady blowing performance for different chordwise positions x/c

at $x/c = 0.75 - 0.8$ enable the largest lift reductions for a given jet momentum, but also produce significant positive change of pitching moment that can have a detrimental effect on actuator effectiveness if aeroelastic effects are taken into account. The jets located at $x/c \leq 0.6$, however, show to some extent a reduced coupling between change of lift and pitching moment. A possible compromise between high lift control authority and low pitching moment influence, and thus a potential candidate actuator with acceptable aeroelastic effectiveness for implementation on a flexible wing, can be found in the actuator located at $x/c = 0.6$.

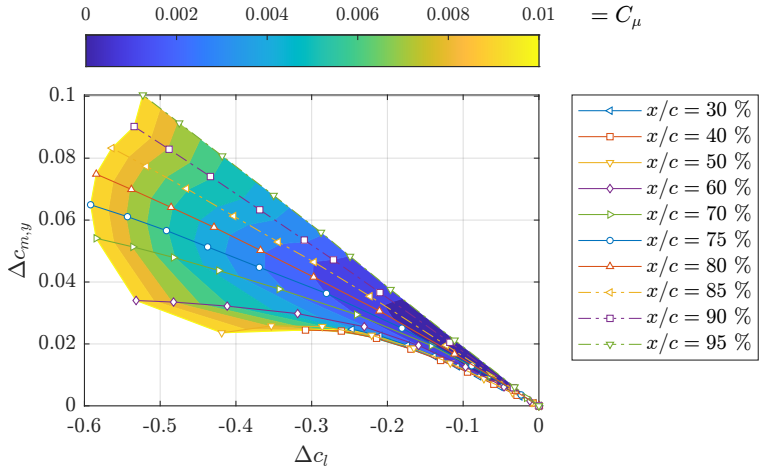

Figure 6: Change of lift and pitching moment for different chordwise positions

A subsequent variation of the slot width in a range of $w/c = 0.025\,\% - 0.5\,\%$ was conducted for the actuator located at $x/c = 0.8$ and tilted at $\theta = 45\,^\circ$ relative to the local wall normal. From a simple consideration of the jet properties defined in Eq. 2, it is well known that for increasing slot width at constant jet momentum and constant jet pressure, the mass flow increases and the jet velocity decreases with the square root of the slot width. The kinetic jet power $\dot{E}_{\text{jet}} = \dot{m} v_{\text{jet}}^2$ increases linearly with the jet velocity. These relations can be observed in Figs. 7a–c, which show the reduction of lift coefficient over mass flow, jet momentum coefficient, and kinetic jet power coefficient for the investigated slot widths. Data points obtained at a similar C_μ but decreased slot width result in lower mass flow rates and higher kinetic power. The required mass flow for the lowest slot width of $w/c = 0.025\,\%$ is reduced by about 50 % compared to the widest slot of 0.5 %c, while the kinetic power increases by an order of magnitude.

The momentum coefficient was historically introduced to eliminate the influence of slot widths on the performance of a blown flap exploiting the Coanda effect.[27] It was experimentally confirmed that the lift change of the blown flap is independent from the slot width if plotted against C_μ. This also holds true for the surface jet actuator investigated in this study, as long as the jet operates at subsonic exhaust velocities. The idealized jet Mach number

$$M_{\text{jet}} = \sqrt{\frac{C_\mu q_\infty A_{\text{ref}}}{\gamma p_\infty A_{\text{jet}}}} \tag{7}$$

depending on the jet momentum for different slot widths is shown in Fig. 7d. In connection with Fig. 7b, it becomes apparent that the lift reduction curves are similar for all subsonic data points, but start to gradually diverge as the jet velocity approaches supersonic conditions. The inflow boundary conditions in the blowing duct are controlled in a way that the jet is ideally expanded to free stream pressure p_∞ for every data point. The divergence of the lift reduction curves is thus not an effect of the pressure term from the C_μ calculation. It may be explained instead by a performance deterioration of the supersonic jet interacting with the cross-flow that leads to an increase in required jet momentum to reach a targeted Δc_l.

The relation between mass flow, jet momentum, and kinetic jet power for different slot widths shows how the slot width can be used as a design parameter to trade-off mass flow demand against power requirement. Depending on which of these quantities is limiting or sizing in the actual flow control system, a wider slot with higher mass flows can be selected in favor of low compressor power demand or vice versa. The kinetic jet power may not be the critical property in case of using engine bleed air stored in a buffer reservoir. The engine's operational constraints in this case depend more strongly on the withdrawal of core mass flow, making mass flow reduction the design driver of the actuator. Also, the interpretation of C_μ as a thrust reduction (see Sec. 2.2) should be kept in mind. A certain diminution of C_μ-efficiency may be accepted to reduce the mass flow demand of the actuator by selecting small slot widths.

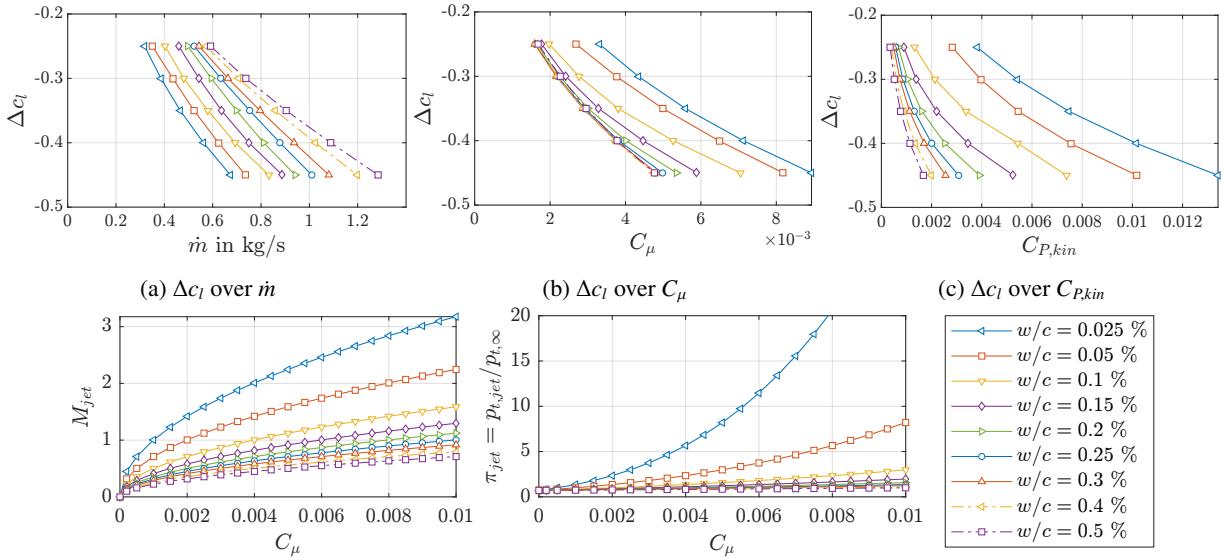

(a) Δc_l over $\dot{m}$ (b) Δc_l over C_μ (c) Δc_l over $C_{P,kin}$

(d) Jet Mach number over C_μ (e) Pressure ratio over C_μ

Figure 7: Lift reduction and jet properties for a variation of slot widths w/c

The total pressure ratio $\pi_{\text{jet}} = p_{t,\text{jet}}/p_{t,\infty}$ that has to be provided to achieve a certain jet momentum for different slot widths is shown in Fig. 7e. It is computed according to Eq. 8 and corresponds to the compression ratio a compressor has to achieve to increase the total pressure of the jet fluid from intake ram pressure $p_{t,\infty}$ to the total pressure $p_{t,\text{jet}}$ at the duct inlet.

$$\pi_{\text{jet}} = \frac{p_{t,\text{jet}}}{p_{t,\infty}} = \frac{p_\infty}{p_{t,\infty}} \left(1 + \frac{\gamma - 1}{2} M_{\text{jet}}^2\right)^{\frac{\gamma}{\gamma-1}} \tag{8}$$

If the blowing air is supplied from engine bleed air, π_{jet} gives the pressure ratio of the compressor stage from which the bleed air is taken. In modern turbofan engines, bleed air is typically extracted from the higher stages of the high pressure compressor at pressure ratios of $10 - 20$.[28] Thus, the available compression ratio imposes a restriction on the smallest slot widths that can be selected. At least for the moderate jet momentum of $C_\mu \leq 0.01$ studied here, realistic compression ratios allow for the implementation of a slot width of $w/c = 0.05\,\%$ with corresponding low mass flow and supercritical jet velocities.

A duct geometry featuring a convergent nozzle with a contraction ratio of 1.2 and a throat width of $w/c = 0.05\,\%$ was chosen based on these design considerations to study the effects of off-design performance for a high-velocity jet actuator. The nozzle is located at $x/c = 0.8$ and tilted by $\theta = 60°$ against the flow. The nozzle chokes at $C_\mu = 0.002$ and generates an under-expanded jet with $p_{\text{jet}} > p_\infty$ for any $C_\mu > 0.002$. The corresponding Mach contour plot with selected streamlines for $C_\mu = 0.005$ is shown in Fig. 8. The supersonic regions of the jet in the zoomed-in inset are enclosed by a black dashed line and an after-expansion of the jet downstream of the throat is clearly visible. Mach numbers of locally up to $M_{\text{jet}} = 1.7$ are reached before the interaction of the jet with the cross-flow leads to the

formation of an oblique shock. The jet stays supersonic and is further deflected by a system of oblique shocks. This is in contrast to the continuous and shock-free deflection of subsonic jets. The entropy-loss experienced across the shock surface may explain the slightly deteriorated capability of supersonic jets to convert their momentum into lift reduction, as discussed above. Nevertheless, the jet has a strong effect on the outer aerodynamics, e.g. reducing the suction peak that is present on the suction side of the unblown airfoil.

The jet performance of the convergent nozzle is compared in the following with the duct with parallel side walls to identify deviations from the ideal-nozzle assumption used for the design study above. The critical mass flow at which sonic speed is reached at the throat of the convergent nozzle is $\dot{m} = 0.3\,\mathrm{kg/s}$ ($C_\mu = 0.002$). Figure 9 shows no difference in lift reduction for subsonic blowing conditions. For supersonic blowing however, the mass flow efficiency gradually deteriorates for the convergent nozzle. The mass flow at supersonic conditions equals the critical mass flow

$$\dot{m}_{\max} = 0.68473 A_{\mathrm{jet}} p_0 \sqrt{R T_0}; \tag{9}$$

for the given reservoir pressure p_0 and temperature T_0. An increase of mass flow is achieved by raising p_0, which leads to a growth in throat pressure $p_{\mathrm{throat}} = p^* = 0.53 p_0$ and thus stronger post-expansion of the jet. The potential of the jet fluid to gain kinetic momentum from its inner enthalpy is taken into account in the C_μ-computation by the pressure term in Eq. 2. The ability of the jet to convert its momentum into lift reduction is not significantly restricted by the post-expansion compared to the ideally expanded jet. Therefore, only small differences in the lift reduction curve over C_μ in Fig. 8b are visible between both nozzles. In other words, the jet is always able to convert its momentum into lift reduction, regardless whether the momentum is already kinetic (ideally expanded jet) or still has to be converted from enthalpy (under-expanded jet) via post-expansion outside of the duct. However, the chocked convergent nozzle requires a higher mass flow to reach the same jet momentum due to the limitation of v_{jet} to sonic speed. The results indicate that the conclusions from the design study shown above can be generalized to realistic nozzles when plotted over C_μ, but the nozzle's off-design behavior has to be taken into account for assertions on mass flow requirements.

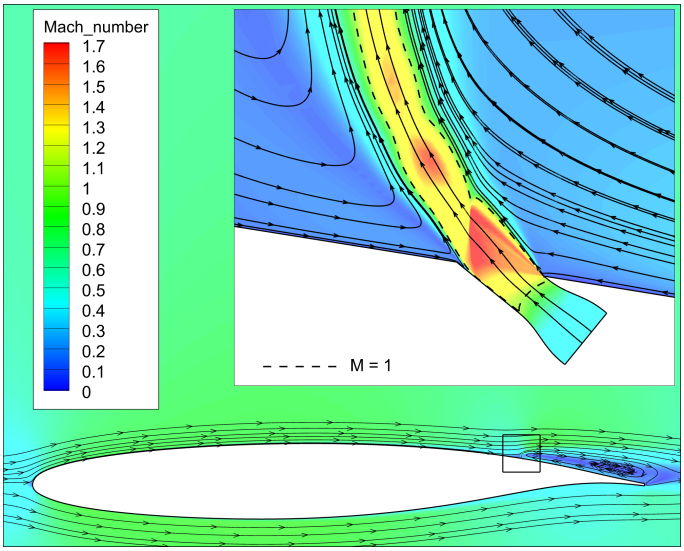

Figure 8: Flow field of the convergent nozzle operated at $C_\mu = 0.005$, $M_\infty = 0.71$, $\alpha = 0°$.

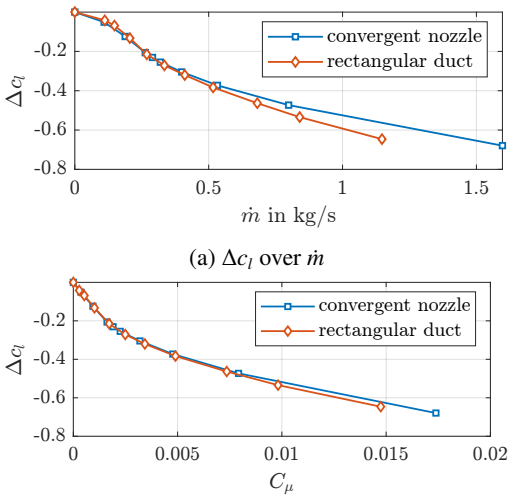

(a) Δc_l over $\dot{m}$

(b) Δc_l over C_μ

Figure 9: Comparison of convergent and ideal nozzle performance.

To conclude this first part of the study, a suitable actuator geometry with corresponding operating conditions to achieve significant lift reduction was established. The identified actuator has reduced requirements on mass flow compared to previous studies, while complying with restrictions from the integration with a realistic supply of pressurized air. Understanding of the coupling between control authority on lift and pitching moment was gained and the effect of narrow/high-velocity jets on actuator performance was analyzed.

3.2 Performance characterization under different flight conditions

Two actuators at different chordwise positions $x/c = 0.8$ and $x/c = 0.6$ were selected for further investigations of their performance at different flight conditions. The geometries were chosen based on the results discussed in Sec. 3.1 and have the same slot width of $w/c = 0.05\,\%$, contraction ratio of 1.2 and tilt angle of $\theta = 60°$ as the actuator shown in

c in m	H in km	M	Re_∞	Re_{2D}
1.63	11.2	0.3	3.6×10^6	3.3×10^6
6.4	0	0.76	1.1×10^8	1.0×10^8

Table 2: Boundary cases for maximal and minimal Reynolds number

Fig. 8. The actuator at $x/c = 0.8$ was selected due to its superior lift reduction at a given C_μ (for a torsionally stiff wing) and the $0.6c$ position was additionally included in the study as a potential candidate with high aeroelastic effectiveness.

First, the effect of Reynolds number is investigated by scaling the model size while keeping freestream velocity, flight altitude and thus Mach number constant. The Reynolds number of the 2D case varies between $Re_{2D} = 10^6 - 10^8$ to include boundary cases of actuator operation as given in Tab. 2. A fully turbulent airfoil was assumed in all cases. The lift coefficients plotted over Reynolds number for different blowing rates are shown in Fig. 10a. They increase with Re as expected due to a decreasing influence of boundary layer thickness. The resulting lift reductions Δc_l, as shown in Fig. 10b, differ by less than 10 % for the lowest Reynolds number and by less than 3 % for $Re \geq 5 \cdot 10^6$. The observed Reynolds number dependency is small enough to be considered as only of secondary importance and will therefore be neglected in the following investigations.

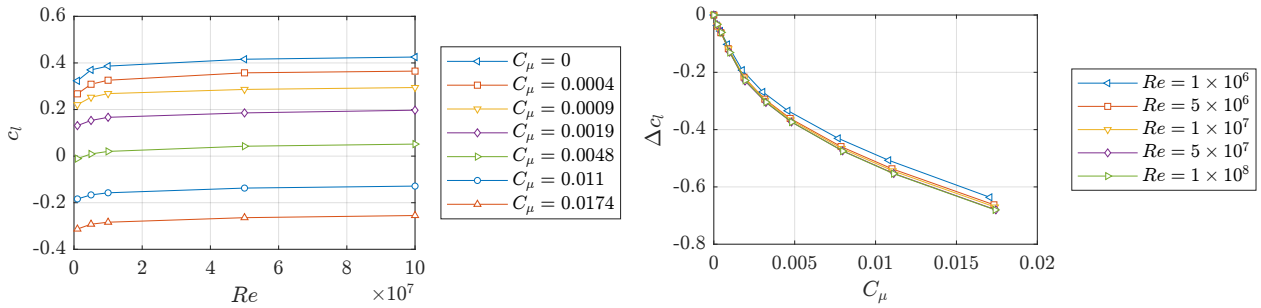

(a) c_l over Re (b) Δc_l over C_μ

Figure 10: Reynolds number effect for an actuator at $x/c = 0.8$, $M_\infty = 0.71$, and $\alpha = 0°$

In a subsequent step, Mach number and angle of attack were varied simultaneously to study the actuator performance at different flight conditions. The Mach number values $M_\infty \in \{0.3, 0.5, 0.71, 0.76\}$ were chosen to cover flight conditions including high-speed cruise, design cruise and low-speed flight. Different angle of attack ranges were selected depending on the Mach number to cover realistic cruise conditions in the linear lift regime as well as high loading conditions around $c_{l,\max}$ that occur during gust and maneuver flight. The angle of attack variation for the highest Mach number does not include values beyond $\alpha(c_{l,\max})$ to avoid cases with shock-induced separation that occurs for these conditions. The altitude was kept constant at the design cruise altitude of $H = 7650$ m to restrict the parameter space. A variation of Mach number therefore also results in a moderate variation in Reynolds number between $Re = 13 - 32 \times 10^6$, which is not further taken into account as discussed above.

A sweep of blowing intensity from no blowing to supersonic blowing at a momentum coefficient of about $C_\mu \approx 0.015$ was performed for all combinations of Mach number and angle of attack. The blowing intensity is controlled by prescribing different total pressures at the inlet boundary, as described in Sec. 2.2. The nozzle pressure ratio $NPR = p_{t,\text{inlet}}/p_\infty$ is thus the control variable and used in the following to indicate blowing intensities.

The isolated effect of angle of attack variation at $M_\infty = 0.71$ is shown in Fig. 11 for the actuator at $x/c = 0.6$. Qualitatively similar results with minor quantitative differences are obtained for the actuator at $x/c = 0.8$. Both actuators show the trend of increasing lift reduction over angle of attack. The negative slopes of the Δc_l-curves shown in Fig. 11a increase with angle of attack in the linear regime. The obtained Δc_l becomes maximal at the angle of attack $\alpha(c_{l,\max,\text{clean}}) \approx 4°$, at which the clean airfoil without blowing reaches its highest lift coefficient, and breaks down for higher α. Figure 11b shows the same effect for the absolute lift coefficients at the respective blowing rate. The lift gradient $dc_l/d\alpha$ decreases with stronger blowing (lower NPR) resulting in a spreading of the lift curves towards $\alpha(c_{l,\max,\text{clean}})$. These findings are in contrast to comparable investigations[13] with a lower resolution of the parameter space suggesting that Δc_l-values would be independent of the angle of attack within the linear regime. An incompressible study[29] on a symmetric wind turbine airfoil even indicated that lift reduction decreases towards $\alpha(c_{l,\max,\text{clean}})$, which was attributed to growing boundary layer thickness on the upper side of the airfoil impairing the actuator effectiveness. This effect is clearly not dominant under the high subsonic and transonic conditions investigated in the

present study. An explanation of the decreasing lift slope shown in Fig. 11b can be found in the violation of the Kutta condition caused by the forced separation between jet and trailing edge. The flow on the upper side of the airfoil is not attached at the trailing edge, which allows the flow on the lower side to deflect slightly upwards at the trailing edge. A comparable effect occurs at thick elliptic airfoils with round trailing edges that do not force the aft stagnation point to a determined location, which results in reduced lift slopes.[30]

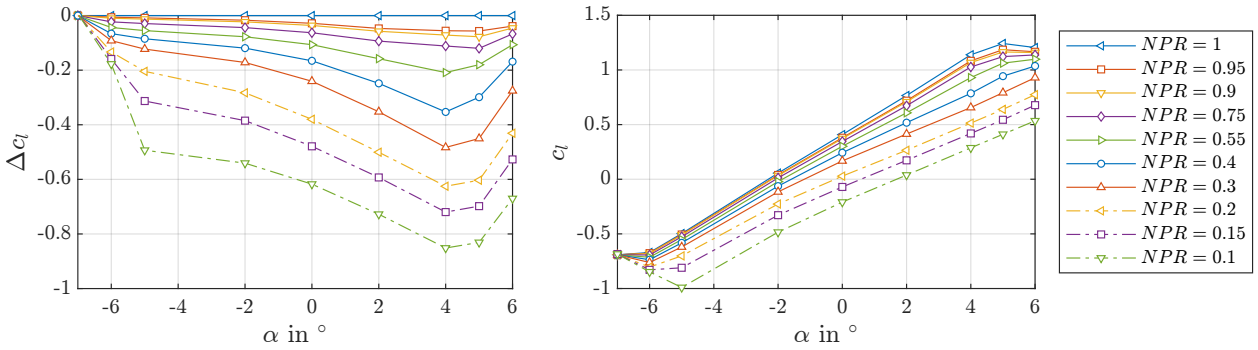

(a) Δc_l over α (b) c_l over α

Figure 11: Angle of attack effect for an actuator at $x/c = 0.6$ and $M_\infty = 0.71$

The resulting changes of lift and pitching moment for $M_\infty \in \{0.5, 0.71, 0.76\}$ and all angles of attack are plotted in Fig. 12 for the actuator located at $x/c = 0.6$ and in Fig. 13 for $x/c = 0.8$. All subfigures show the values obtained from the CFD simulation as circles as well as the fitted data of the surrogate model as crosses connected by solid lines. The optimized fitting parameters for $M_\infty \in \{0.3, 0.5, 0.71, 0.76\}$, and Δc_l, Δc_d and $\Delta c_{m,y}$ are documented in appendix Table 3 and appendix Table 4. The CFD data is generally well represented by the fitted model, while some regions of the parameter space revealed challenges in the modeling. A more detailed discussion of the fitting quality is given at the end of this section. The Mach number $M_\infty = 0.3$ was also simulated and modeled but is not shown here as it yields very similar results as $M_\infty = 0.5$.

Direct comparison between the actuator locations for all Mach numbers reveals that the actuator at $x/c = 0.6$ produces a steeper gradient of Δc_l with respect to angle of attack. The lift reductions obtained at $\alpha = 0°$ for all Mach numbers are smaller than those of the jet at $x/c = 0.8$, as stated before in Sec. 3.1. The maximum values of Δc_l obtained at the stall angle of the clean airfoil, however, are comparable for both actuators. This is especially remarkable as the corresponding changes in pitching moment of the more forward located actuator are significantly lower than those of the more rearward actuator. Hence, an increased aeroelastic effectiveness of actuators located at $x/c = 0.6$ is expected, which will be discussed for different spanwise locations in Sec. 3.3. The change of pitching moment increases with Mach number for both actuators, which can pose a challenge for the aeroelastic effectiveness at high-speed flight.

Another difference between both actuator locations is observed at $M = 0.76$ for high angles of attack: While the effect on lift and pitching moment of the actuator at $x/c = 0.8$ drops quickly for $\alpha > 2°$, it remains more stable for the more forward actuator. This actuator operates in a region where the flow of the clean airfoil is not yet separated, and it can therefore still significantly affect the supersonic region, mitigate its magnitude and move the shock forward so that pressure footprint and correspondingly lift are reduced. In contrast, the rearward actuator operates in a region that is already separated on the clean airfoil. It has to eject a larger mass flow to create an effect beyond the already existing separation, causing a notable degradation of control authority.

Figure 14 shows the mean fitting error for the actuator positioned at $x/c = 0.6$ and $x/c = 0.8$. The error is averaged over all available NPRs per angle of attack and Mach number, where the number of NPRs is denoted as n_{NPR}. This comparison is visualized for both lift and moment coefficient. Figure 14a and 14b show absolute

$$e_{Abs}(\Delta c_X(\alpha, M_\infty)) = \left(\sum_{i=1}^{n_{NPR}(\alpha, M_\infty)} \left| \Delta c_X^{CFD}(\alpha, NPR(i), M_\infty) - \Delta c_X^{Fit}(\alpha, NPR(i), M_\infty) \right| \right) (n_{NPR}(\alpha, M_\infty))^{-1} \tag{10}$$

and relative

$$e_{Rel}(\Delta c_X(\alpha, M_\infty)) = \frac{e_{Abs}(\Delta c_X(\alpha, M_\infty))}{\max\limits_{NPR} \left(\left| \Delta c_X^{CFD}(\alpha, NPR, M_\infty) \right| \right)} \tag{11}$$

values, respectively. The errors in Eq. 11 are computed relative to the largest absolute aerodynamic coefficient over all available NPRs per angle of attack and Mach number $\max\limits_{NPR} \left(\left| \Delta c_X^{CFD}(\alpha, NPR, M_\infty) \right| \right)$.

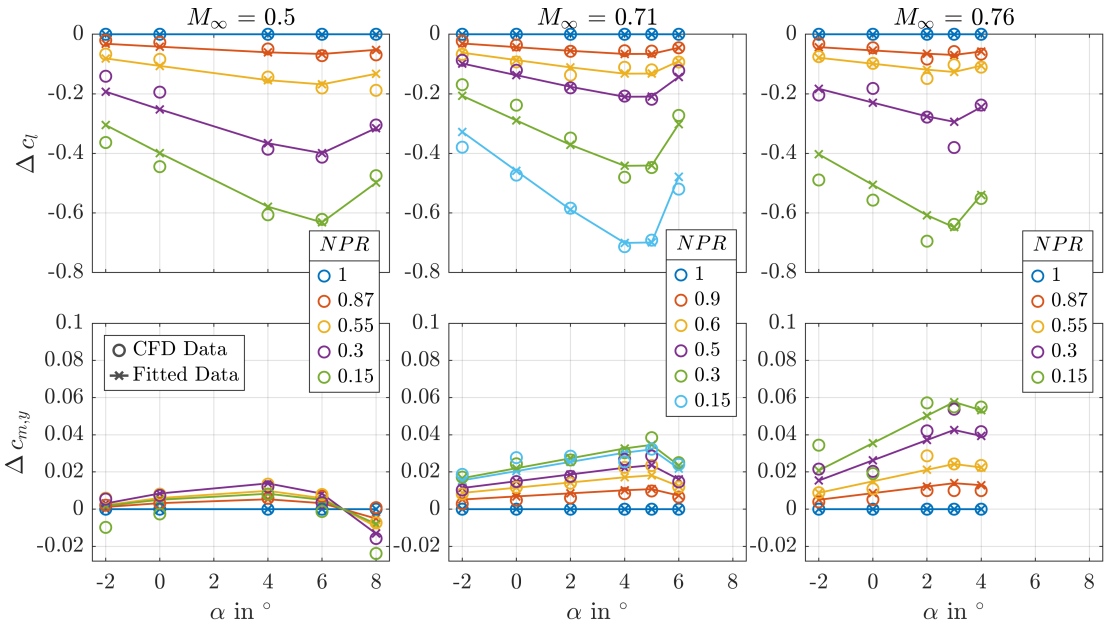

Figure 12: Surface jet aerodynamic coefficients over angle of attack at $x/c = 0.6$, fitted and CFD data

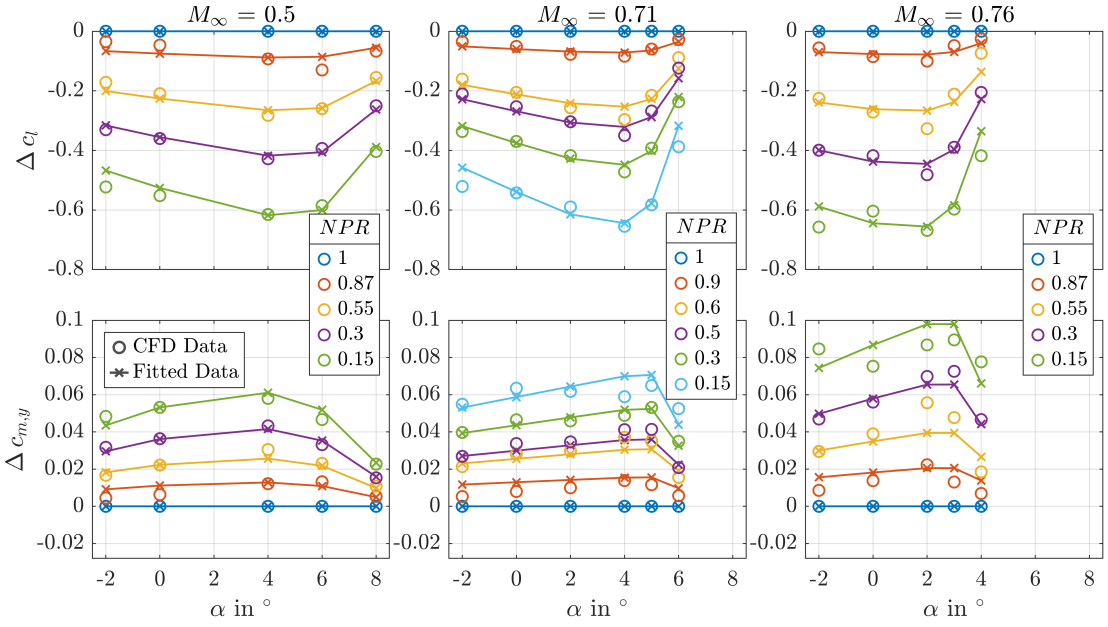

Figure 13: Surface jet aerodynamic coefficients over angle of attack at $x/c = 0.8$, fitted and CFD data

The fitting function is parameterized to best represent the CFD data of the lift coefficient, resulting in a larger relative fitting error for the moment coefficient. The CFD data for the largest M_∞ are scattered more, which affects the overall quality of the fit. There is a large relative error for the pitching moment at $\alpha = -2°$ and $\alpha = 8°$ of the actuator positioned at $x/c = 0.6$ at $M_\infty = 0.5$ as the given data points cannot be represented by the candidate function, refer to Fig. 12 and Fig. 16. However, this deviation is conservative and the relative error is additionally elevated due to the small absolute values. Overall, the fitted reduced order models represent the aerodynamic coefficients of the two surface jets sufficiently well for the subsequent investigation on aeroelastic effectiveness that is carried out at a small angle of attack (trimmed horizontal flight).

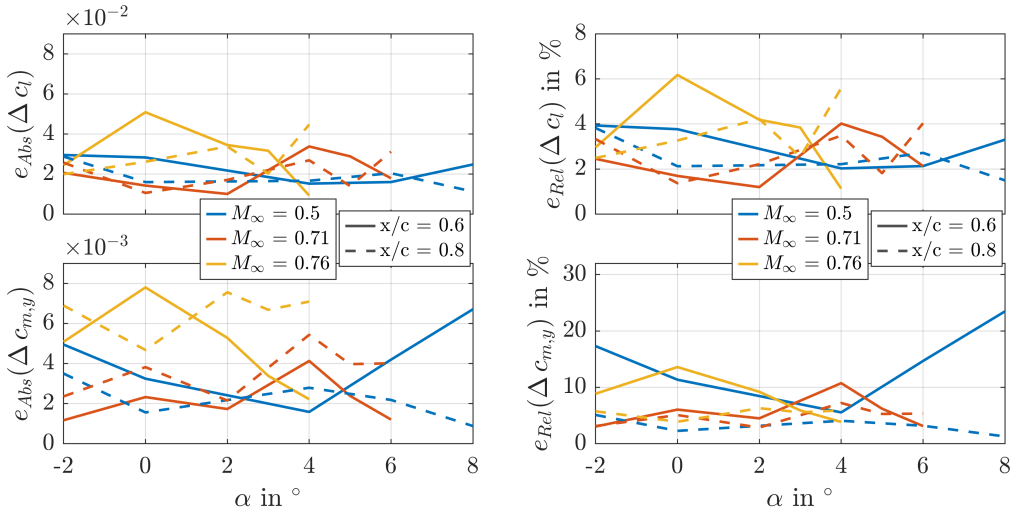

(a) Absolute fitting error

(b) Relative fitting error

Figure 14: Mean absolute fitting error per angle of attack, averaged over NPR

3.3 3D integration and aeroelastic effects

The results shown so far relate to a 2D airfoil without elastic deformation. To investigate the actuator performance on a flexible 3D wing, the surface jets positioned at $x/c \in \{0.6, 0.8\}$ are implemented in the aeroelastic framework presented in Sec. 2.4 and tested regarding their aeroelastic effectiveness for the aircraft configuration presented in Sec. 2.1. For this investigation, the aircraft is trimmed at $M_\infty \in \{0.5, 0.76\}$ and an altitude of 6000 m. Furthermore, rigid body accelerations in rotation and translation are suppressed. This approach is similar to a conventional wind tunnel setup for a constant angle of attack and provides a consistent testing environment.

The aeroelastic effectiveness of wing actuators can be characterized by various quantities. A change in wing root bending moment relative to its trim value $\Delta WRBM\,/\,WRBM_{Trim}$ is utilized here. Figures 15a and 15b show $\Delta WRBM\,/\,WRBM_{Trim}$ over increasing actuation (mass flow for surface jet, deflection angle δ_A for ailerons) for $M_\infty \in \{0.5, 0.76\}$, respectively. The actuator types are indicated by color, and the spanwise position of the actuator section is indicated by the line style. Figures 15c and 15d provide insight into the effect of the elastic wing twist on actuator effectiveness by showing the aeroelastic effectiveness with suppressed actuator pitching moment, representing a torsionally stiffer wing.

The wing actuators are employed symmetrically on the aircraft in this study, one set at a time. A maximum aileron deflection of 10° is assumed due to the high operating velocities. The surface jets deplete a mass flow of up to 1.5 kg/s per actuator section, which is based on Shmilovich et al.,[31,32] where an available mass flow of up to 1.6 kg/s is assumed (drawn from engine core or auxiliary power unit). The three spanwise actuator sections are defined such that the individual sections influence the same reference wing area, i.e., the product of average chord and spanwise length is kept constant. This ensures comparability of individual surface jet effectiveness over varying actuation. Correspondingly, the surface jet sections have a length of $\{3.1, 2.6, 2.2\}$ m. The choice of spanwise surface jet section length can lead to 3D effects on the actuator performance either due to varying slot width or because of longitudinal vortices generated at the lateral ends of the slots. Such effects are not considered in the employed simulations. In this study, only the spanwise position of the wing actuators are investigated. Thus, there is a research opportunity for future studies to optimize the section length of surface jets based on high fidelity coupled simulations that are capable of modeling such effects.

The spanwise position of the actuator section has several, in some cases opposing, effects: Placing the actuator section more outboard increases the lever arm with respect to the wing root, but the affected part of the spanwise lift distribution has lower absolute lift values due to wing taper and spanwise downwash towards the wing tip. Furthermore, the outer wing section is naturally more subjected to twist and bending deformation. These effects are considered by the aeroelastic model and result in the different aeroelastic effectiveness curves for each spanwise position of the actuator sections in Fig. 15. The midboard section is the most effective spanwise position in all cases, closely followed by the inboard section, and the outboard section is the least effective. The only exception to this order is at $M_\infty = 0.76$ for the ailerons, where the inboard section is the most effective. One reason for the larger sensitivity on the spanwise position is the increased pitching moment of the ailerons compared to the surface jets. That is, actuators with large pitching

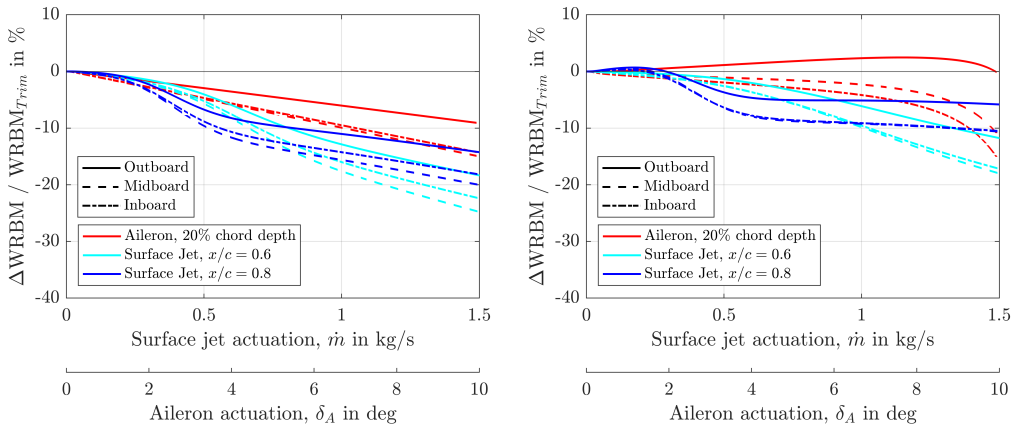

(a) WRBM change, $M_\infty = 0.5$ (b) WRBM change, $M_\infty = 0.76$

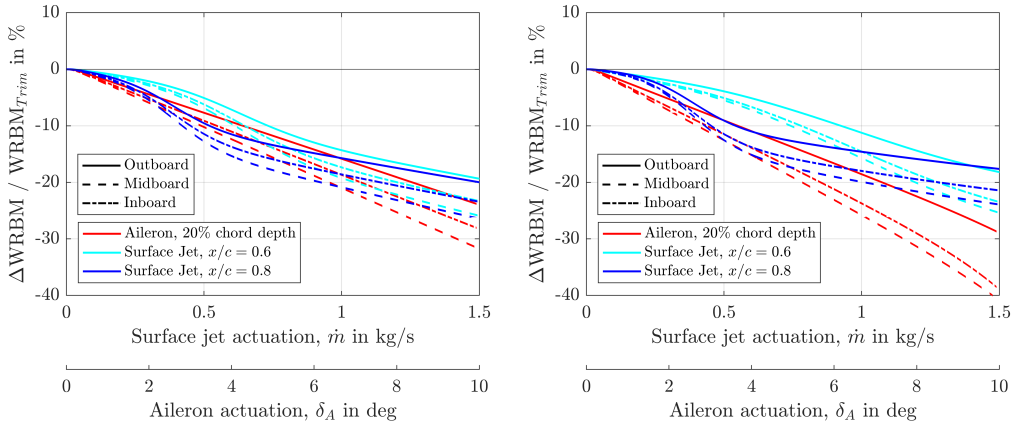

(c) WRBM change, $M_\infty = 0.5$, Actuator $\Delta c_{m,y} = 0$ (d) WRBM change, $M_\infty = 0.76$, Actuator $\Delta c_{m,y} = 0$

Figure 15: Aeroelastic effectiveness of surface jets compared to ailerons for three wingspan positions

moment should be placed more inboard where the wing is more torsionally stiff.

All actuators have acceptable aeroelastic effectiveness in the subsonic test case, see Fig. 15a. The surface jet positioned at $x/c = 0.8$ is more effective at the respective spanwise position up to a mass flow of 0.8 kg/s. At larger mass flows, the forward positioned surface jet becomes more effective due to its reduced pitching moment, cf. Fig. 15a/15c. The large pitching moment of the ailerons render them the least effective actuators for each spanwise position and large actuation ($\dot{m} > 0.5$ kg/s, $\delta_A > 3°$) in Fig. 15a. If the wing was torsionally stiff, the ailerons would be the most effective for the given example, see Fig. 15c.

Increasing the free stream Mach number to transonic conditions results in deteriorated aeroelastic effectiveness, cf. Fig. 15a/15b, due to the over-proportionally increased pitching moment for both ailerons and the two investigated surface jets, recall Fig. 12 and Fig. 13. This over-proportional penalty is also observable by comparing Fig. 15b/15d to Fig. 15a/15c. The outboard ailerons even work in reverse in Fig. 15b. At low mass flows $\dot{m} < 0.3$ kg/s, the rearward positioned surface jet also experiences control reversal at all spanwise positions. For moderate mass flows of $0.3\,\text{kg/s} < \dot{m} < 0.9\,\text{kg/s}$, the rearward positioned surface jet remains more effective at all spanwise positions, like in the subsonic test case. However, the control authority of the rearward positioned surface jet stagnates for larger mass flows $\dot{m} > 0.7$ kg/s, ultimately rendering the forward positioned surface jet more effective at all spanwise positions. This implies that a more forward positioned surface jet is more suitable for active load alleviation on a torsionally soft wing in transonic operating conditions if a sufficient mass flow is available. Further, for a torsionally soft wing, surface jet actuators can outperform classical trailing edge flaps in terms of control authority. Overall, the aeroelastic effectiveness is highly dependent on the structural stiffness, see Fig. 15a/15b versus Fig. 15c/15d. While this study indicates the sensitivities of the actuator placement, a full load alleviation system would likely require actuation over a larger spanwise extent. It is expected that a combination of multiple spanwise segments results in load alleviation exceeding the currently demonstrated 10-20 % in trim WRBM reduction but also requires larger mass flows. Note that load reduction for realistic load cases still needs to be examined as different instantaneous angles of attack and required short actuation times can drastically affect the outcome of the load alleviation.

4. Conclusions

The present work investigates surface jets for lift reduction, as these actuators provide an effective and fast-reacting method for load alleviation. Two main objectives were pursued in this paper. First, the actuator's mass flow demand was to be minimized. Second, actuator integration on a three-dimensional elastic wing was investigated regarding control authority under consideration of aeroelastic effects. A parametric study on 2D actuator design was carried out based on RANS simulations on a representative wing section of a medium range transport aircraft. Selected actuator geometries were subsequently investigated regarding their performance under various flight conditions. A comprehensive CFD dataset of Reynolds number, Mach number, and angle of attack variation was generated and a reduced order model derived. The model was implemented in a low-fidelity aeroelastic framework to study three-dimensional aeroelastic effects of the actuator and sensitivities regarding spanwise positioning.

The importance of the slot width as a design parameter to balance mass flow against jet velocity and thus compressor power was discussed. For a constraint pressure ratio, the mass flow demand can be reduced by about 40 % compared to earlier studies by employing a slot width of 0.05 % relative to the chord length. A reduction of actuator efficiency regarding jet momentum has to be taken into account for supersonic jet velocities.

Regarding the second objective, a variation of chordwise position showed that an actuator located at 80 % of the chord length provides the highest lift reductions under cruise flight conditions but also significant nose-up pitching moment. This leads to reduced aeroelastic effectiveness on a flexible wing compared to an actuator located at 60 % of the chord length. The more forward located actuator has a significantly lower pitching moment influence at only slightly impaired authority on lift reduction. This combination enables it to achieve around 20 % reduction of wing root bending moment relative to the cruise value in both subsonic and transsonic flight at a mass flow rate below 1.5 kg/s. The rearward positioned actuator, however, outperforms its forward counterpart at low blowing rates, especially when located further inboard. Conventional ailerons yield less wing root bending moment reduction due to their increased pitching moment causing an adverse wing twist. The sensitivity analysis on spanwise positioning showed for both chordwise positions that an optimal location is found at the second most outboard actuator section investigated here (reaching from 69 % to 81 % half-span). This position offers a good balance of spanwise lever arm and impact on the lift distribution on the one side to reduce the bending moment, as well as performance reduction on the other side due to twist deformation and 3D effects towards the wing tip.

The study highlights the importance of considering the actuator induced pitching moment and the wing's twist-bending coupling when designing actuators for flexible wings in transonic operating conditions. Future studies using CFD-CSM coupled simulations will further investigate spanwise actuator positioning and sizing for effective alleviation of gust induced loads.

5. Acknowledgments

We would like to acknowledge the funding by the Deutsche Forschungsgemeinschaft (DFG, German Research Foundation) under Germany's Excellence Strategy - EXC 2163/1 - Sustainable and Energy Efficient Aviation - Project-ID 390881007.

We also gratefully acknowledge the computing time made available on the high-performance computer "Lise" at the NHR Center NHR@ZIB. This center is jointly supported by the Federal Ministry of Education and Research and the state governments participating in the NHR.

References

[1] Liu, Y., Elham, A., Horst, P., and Hepperle, M., "Exploring Vehicle Level Benefits of Revolutionary Technology Progress via Aircraft Design and Optimization," *Energies*, Vol. 11, No. 1, 2018, pp. 166.

[2] European Aviation Safety Agency, "Certification Specifications for Large Aeroplanes (CS-25)," 2007-09-19.

[3] Karpuk, S., Liu, Y., and Elham, A., "Multi-Fidelity Design Optimization of a Long-Range Blended Wing Body Aircraft with New Airframe Technologies," *Aerospace*, Vol. 7, No. 7, 2020, pp. 87.

[4] Wunderlich, T. F., Dähne, S., Reimer, L., Schuster, A., and Brodersen, O., "Global Aero-Structural Design Optimization of More Flexible Wings for Commercial Aircraft," *AIAA Aviation 2020 Forum*, AIAA 2020-3170, 2020.

[5] Hahn, D., Haupt, M., and Heimbs, S., "Passive Load Alleviation by Nonlinear Stiffness of Airfoil Structures," *AIAA SCITECH 2022 Forum*, AIAA 2022-0318, 2022.

[6] Thel, S., Hahn, D., Haupt, M., and Heimbs, S., "A passive load alleviation aircraft wing: topology optimization for maximizing nonlinear bending–torsion coupling," *Structural and Multidisciplinary Optimization*, Vol. 65, No. 5, 2022.

[7] Breitenstein, C., Müller, J., Hillebrand, M., Woidt, M., Haupt, M., and Radespiel, R., "Fluid-Structure Coupled Analysis of Maneuver Load Alleviation on a Large Transport Aircraft," *AIAA Aviation 2023 Forum*, AIAA 2023-3953, 2023.

[8] Hillebrand, M., Müller, J., and Lutz, T., "Active Gust Alleviation on a High Aspect Ratio Wing Based on High Fidelity CFD Simulations," *AIAA Aviation 2023 Forum*, AIAA 2023-4347, 2023.

[9] Hillebrand, M., Breitenstein, C., and Lutz, T., "Aeroelastic Effects of a Load Alleviation System on a High Aspect Ratio Wing Based on CFD-CSM Simulations," *AIAA Aviation Forum and Ascend 2024*, AIAA 2024-3841, 2024.

[10] Asaro, S., Khalil, K., and Bauknecht, A., "Unsteady Characterization of Fluidic Flow Control Devices for Gust Load Alleviation," *New results in numerical and experimental fluid mechanics XIII: Contributions to the 22nd STAB/DGLR Symposium*, edited by A. Dillmann, G. Heller, E. Krämer, and C. Wagner, Vol. 151 of *Notes on Numerical Fluid Mechanics and Multidisciplinary Design*, Springer, Cham (CH), 2021, pp. 153–163.

[11] Düssler, S., Siebert, F., and Bauknecht, A., "Coandă-Type Flow Actuation for Load Alleviation," *Journal of Aircraft*, Vol. 59, No. 5, 2022, pp. 1303–1319.

[12] Khalil, K. and Bauknecht, A., "Fluidic Flow Control Devices for Gust Load Alleviation," *Journal of Aircraft*, Vol. 61, No. 4, 2024, pp. 1–14.

[13] Khalil, K., Asaro, S., and Bauknecht, A., "Active Flow Control Devices for Wing Load Alleviation," *Journal of Aircraft*, Vol. 59, No. 2, 2022, pp. 458–473.

[14] Xue, C., Deng, F., Wang, H., and Qin, N., "Aerodynamic Load Reduction on a Supercritical Airfoil Using Tilted Microjets," *International Journal of Aerospace Engineering*, Vol. 2023, 2023, pp. 1–20.

[15] Li, Y. and Qin, N., "Gust load alleviation by normal microjet," *Aerospace Science and Technology*, Vol. 117, 2021, pp. 106919.

[16] Karpuk, S., Radespiel, R., and Elham, A., "Assessment of Future Airframe and Propulsion Technologies on Sustainability of Next-Generation Mid-Range Aircraft," *Aerospace*, Vol. 9, No. 5, 2022, pp. 279.

[17] Wild, J., Pott-Pollenske, M., and Nagel, B., "An Integrated Design Approach for Low Noise Exposing High-Lift Devices," *3rd AIAA Flow Control Conference*, AIAA 2006-2843, 2006.

[18] Shmilovich, A. and Whalen, E. A., "A technique for low input flow control actuation," *AIAA Aviation 2017 Forum*, AIAA 2017-3040, 2017.

[19] Radespiel, R., Burnazzi, M., Casper, M., and Scholz, P., "Active flow control for high lift with steady blowing," *The Aeronautical Journal*, Vol. 120, No. 1223, 2016, pp. 171–200.

[20] Schwamborn, D., Gerhold, T., and Heinrich, R., "The DLR TAU-code: Recent applications in research and industry," *ECCOMAS CFD Conference*, 2006.

[21] Allmaras, S. R., Forrester, J. T., and Spalart, P. R., "Modifcations and Clarifications for the Implementation of the Spalart-Allmaras Turbulence Model," *7th International Conference on Computational Fluid Dynamics*, ICCFD7-1992, 2012.

[22] Beyer, Y., Cavaliere, D., Bramsiepe, K., et. al, "An Aeroelastic Flight Dynamics Model for Gust Load Alleviation of Energy-Efficient Passenger Airplanes," *AIAA AVIATION Forum*, AIAA 2023-4452, 2023.

[23] Beyer, Y., *Active Gust Load Alleviation with Boosted Incremental Nonlinear Dynamic Inversion: Modeling, Control, and Simulation of a Flexible Airplane: Dissertation*, Vol. 19 (2024) of *Berichte aus der Luft- und Raumfahrttechnik*, Niedersächsisches Forschungszentrum für Luftfahrt, Braunschweig, 2024.

[24] Brockhaus, R., *Flugregelung*, Springer, 3rd ed., 2001, ISBN: 978-3-540-41890-0.

[25] Leishman, J. G., "Unsteady lift of a flapped airfoil by indicial concepts," *Journal of Aircraft*, Vol. 31, No. 2, 1994, pp. 288–297.

[26] Al-Battal, N. H., Cleaver, D. J., and Gursul, I., "Lift reduction by counter flowing wall jets," *Aerospace Science and Technology*, Vol. 78, 2018, pp. 682–695.

[27] Poisson-Quinton, P. and Lepage, L., "Survey of French research on the control of boundary layer and circulation," *Boundary Layer and Flow Control: Its Principles and Application*, edited by G. V. Lachmann, Vol. 1, Pergamon Press, New York, 1961, pp. 21–73.

[28] Bräunling, W. J. G., *Flugzeugtriebwerke: Grundlagen, Aero-Thermodynamik, ideale und reale Kreisprozesse, thermische Turbomaschinen, Komponenten, Emissionen und Systeme*, Springer-Vieweg, Berlin Heidelberg, 4th ed., 2015, ISBN: 978-3-642-34539-5.

[29] Blaylock, M., Chow, R., Cooperman, A., and van Dam, C. P., "Comparison of pneumatic jets and tabs for Active Aerodynamic Load Control," *Wind Energy*, Vol. 17, No. 9, 2014, pp. 1365–1384.

[30] Abramson, J., Rogers, E. O., and David, W., "High-speed characteristics of circulation control airfoils," *AIAA 21s Aerospace Sciences Meeting*, AIAA-83-0265, 1983.

[31] Shmilovich, A., Yadlin, Y., Dickey, E. D., Hartwich, P. M., and Khodadoust, A., "Development of an Active Flow Control Technique for an Airplane High-Lift Configuration," *55th AIAA Aerospace Sciences Meeting*, 2017.

[32] Shmilovich, A., "Unconventional Applications and New Approaches for Flow Control," *Fundamentals of High Lift for Future Civil Aircraft*, edited by R. Radespiel and R. Semaan, Vol. 145 of *Notes on Numerical Fluid Mechanics and Multidisciplinary Design*, Springer, Cham, 2021, pp. 3–19.

Appendix

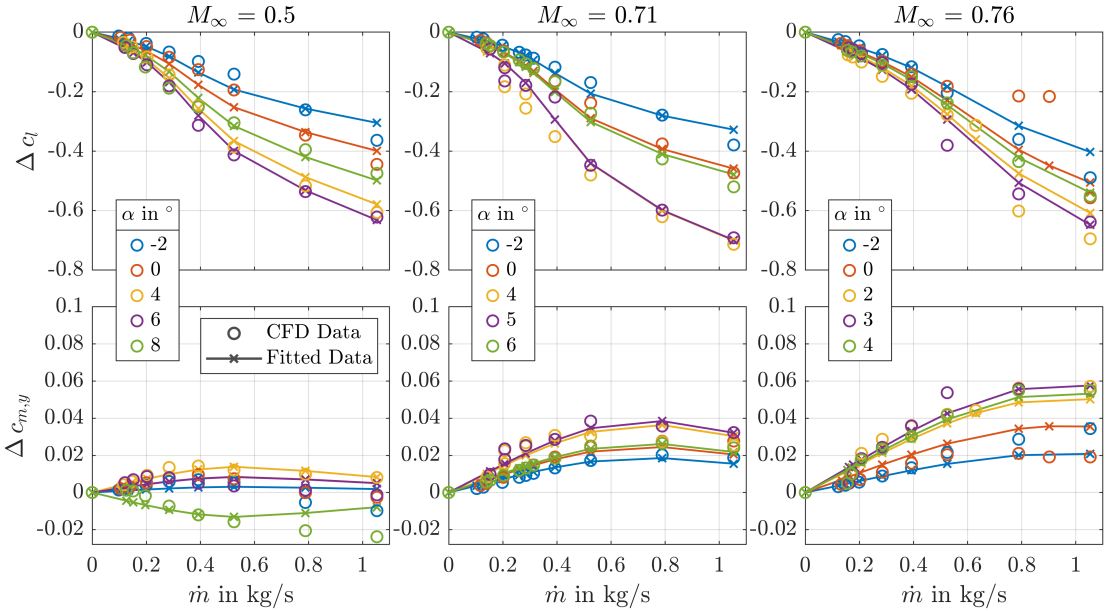

Figure 16: Surface jet aerodynamic coefficients over mass flow at $x/c = 0.6$, fitted and CFD data

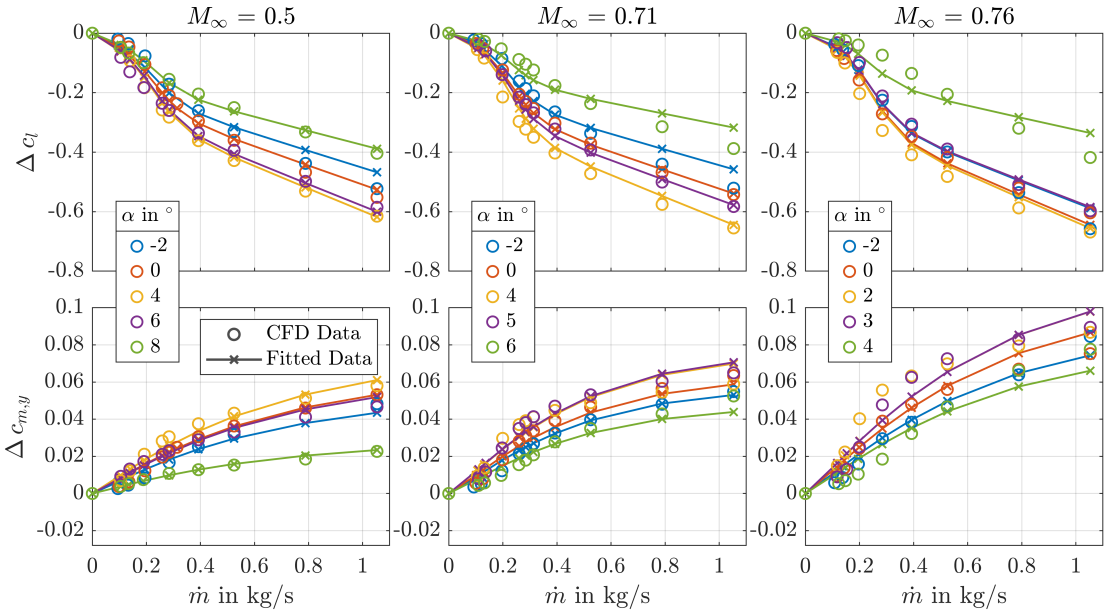

Figure 17: Surface jet aerodynamic coefficients over mass flow at $x/c = 0.8$, fitted and CFD data

Table 3: **Fitting parameters for aerodynamic coefficients of surface jet positioned at x/c=0.6**

Parameter	p_1	p_2	p_3	p_4	p_5	p_6	p_7	p_8
$M_\infty = 0.3$								
Δc_l	-0.3613	0.2317	8.077	-1.092	-0.2883	0.08476	0.6796	14.68
Δc_d	-0.003883	0.192	6.665	-3.885	0.004614	0.1682	0.4587	13.2
$\Delta c_{m,y}$	0.03811	0.2358	8.532	0.000542	1.016e-05	0.1202	0.9735	13.57
$M_\infty = 0.5$								
Δc_l	-0.1849	0.3536	5.463	-1.017	-0.2327	0.1182	0.8494	8.424
Δc_d	-0.00405	0.3609	5.446	-3.399	0.004439	0.2134	0.7824	7.47
$\Delta c_{m,y}$	0.03058	0.6396	2.515	0.000475	0.006591	0.313	0.4289	4.334
$M_\infty = 0.71$								
Δc_l	-0.1882	0.3851	5.208	-1.27	-0.2369	0.1429	1.449	6.141
Δc_d	-0.004041	0.4751	5.258	-2.269	0.003043	0.1545	0.7051	4.376
$\Delta c_{m,y}$	0.05413	0.8725	2.224	0.0004902	0.02281	0.1213	2.943	6.141
$M_\infty = 0.76$								
Δc_l	-0.2669	0.5671	3.647	-1.199	-0.304	0.1017	2.645	4.408
Δc_d	0.0126	1.058	42.26	-5.052	0.006448	0	0.3547	2.926
$\Delta c_{m,y}$	0.05993	1.156	1.969	0.0004716	0.05632	0.2071	8.06	4.137

Table 4: **Fitting parameters for aerodynamic coefficients of surface jet positioned at x/c=0.8**

Parameter	p_1	p_2	p_3	p_4	p_5	p_6	p_7	p_8
$M_\infty = 0.3$								
Δc_l	-0.9353	0.3361	6.375	-1.151	-0.4109	0.03406	0.3707	15.82
Δc_d	0.692	1.599	1.585	0.07984	1.237	0.005803	0.000619	15
$\Delta c_{m,y}$	0.103	0.6596	1.452	-0.6331	0.05128	0.04395	0.5126	13.08
$M_\infty = 0.5$								
Δc_l	-0.2783	0.2238	8.249	-0.818	-0.3208	0.05687	0.6272	8.524
Δc_d	0.0354	0.8851	1.844	0.5384	0.0132	0.1403	0.5006	6.234
$\Delta c_{m,y}$	0.1788	0.07201	0.8072	0.0008583	0.03502	0.1083	0.3122	6.744
$M_\infty = 0.71$								
Δc_l	-0.09787	0.213	8.495	-0.9153	-0.3076	0.07621	1.026	6.136
Δc_d	0.2308	1.343	0.7283	-0.2013	0.005712	0.08989	0.1068	0.8386
$\Delta c_{m,y}$	0.2016	0.1534	0.8876	0.0008109	0.03074	0.04832	2.625	6.233
$M_\infty = 0.76$								
Δc_l	-0.1387	0.2269	8.276	-0.8416	-0.3911	0.04814	1.003	4.387
Δc_d	6.63	1.708	1.005	0.3869	0.09698	0.01824	0.01909	0.1003
$\Delta c_{m,y}$	0.2493	0.1408	0.6316	0.0007686	0.03422	0.07123	1.828	4.355